Imaging snake orbits at graphene *n*-*p* junctions

K. Kolasiński, A. Mreńca-Kolasińska, and B. Szafran

AGH University of Science and Technology, Faculty of Physics and Applied Computer Science, al. Mickiewicza 30, 30-059 Kraków, Poland

We consider conductance mapping of the snake orbits confined along the *n*-*p* junction defined in graphene by the electrostatic doping in the quantum Hall regime. We explain the periodicity of conductance oscillations at the magnetic field and the Fermi energy scales by the properties of the *n*-*p* junction as a conducting channel. We evaluate the conductance maps for a floating gate scanning the surface of the device. In the quantum Hall conditions the currents flow near the edges of the sample and along the *n*-*p* junction. The conductance mapping resolves only the *n*-*p* junction and not the edges. The conductance oscillations along the junction are found in the maps with periodicity related to the cyclotron orbits of the scattering current. Stronger probe potentials provide support to localized resonances at one of the sides of the junction with current loops that interfere with the *n*-*p* junction currents. The interference results in a series of narrow lines parallel to the junction with positions that strongly depend on the magnetic field through the Aharonov-Bohm effect. The consequences of a limited transparency of finite-width *n*-*p* junctions are also discussed.

I. INTRODUCTION

The gapless band structure of graphene allows for electrical doping with formation of *n*-type and *p*-type regions defined by external potentials [1]. With the electron mean-free path [2,3] of several μm, the *n*-*p* junctions [4–6] in graphene are an attractive playground for studies of electron optics [7–12] implemented in the solid state. In particular, the *n*-*p* junctions in the quantum Hall conditions [5,13–15] form waveguides [16] for electron currents, which in the semiclassical picture go along snake orbits [10,17–28] formed by inversion [29] of the orientation of the Lorentz force [30] with the carriers passing across the junction from the conductance to the valence band.

In this work we consider the possibility of mapping the snake orbits confined along the *n*-*p* junction using scanning gate microscopy [31–37] (SGM). The SGM microscopy [31–37] with a charged tip of an atomic force microscope floating above the sample allows one to probe the quantum transport properties of devices with a spatial resolution. Cyclotron and skipping orbits—which are related to the snake orbits by the magnetic deflection—have already been experimentally resolved [36,37] for magnetic focusing [12,24,38–41] of electron currents in unipolar graphene sheets.

For the purpose of the present work we consider a four-terminal cross junction—a geometry of a quantum Hall bar studied previously both by experiment [3,11,42–44] and theory [17,24] of ballistic transport in graphene. We determine the transport properties of the *n*-*p* junction defined within the sample using the atomistic tight-binding approach. We find the characteristic conductance oscillations [10,24,25,25,40] as a function of the magnetic field that are identified with formation of snake orbits. The experimental conductance oscillations can be exactly reproduced by a coherent quantum transport simulation as shown in Ref. [25]. In this work we explain the periodicity of the conductance oscillations by the details of the dispersion relation of the *n*-*p* junction waveguide [8,45] as due to superposition of the junction modes producing scattering density oscillations of the largest wavelength. A perfect agreement with the results of the quantum transport simulation is found in the entire quantum Hall regime.

We demonstrate that the potential of the scanning probe produces variation of the sample conductance but only when the probe floats above the *n*-*p* junction. The probe deflects the electron paths changing the destination terminal of the electron currents and thus affecting the conductance. Outside the junction the sample does not react to the probe as the backscattering is suppressed in the quantum Hall conditions. Although the electron paths are not as clearly resolved as for the magnetically focused trajectories [36,37], the period of the conductance oscillations along the junction is close to the length of the snake orbit period. For stronger tip potentials series of resonances are found on the lines parallel to the junction—but only on one of its sides—where the tip potential supports formation of the quasibound states. For these resonances a current loop is found around the probe which interferes with the wave function flow along the junction waveguide.

II. THEORY

A. Model Hamiltonian

We consider a four-terminal cross structure which is depicted in Fig. 1(a). We use the tight-binding Hamiltonian

$$\boldsymbol{H} = \sum_{k} U_k(\mathbf{r}_k)\boldsymbol{c}_k^\dagger \boldsymbol{c}_k + \sum_{\langle i,j \rangle} t_{ij}\boldsymbol{c}_i^\dagger \boldsymbol{c}_j + \text{H.c.}, \qquad (1)$$

where the second summation denotes the nearest-neighbor pairs and $U_k(\mathbf{r}_k)$ is the external on-site potential energy on the kth site in the lattice. The magnetic field is taken into account by the Peierls substitution

$$t_{ij} = t \exp\left(\frac{2\pi e i}{h} \int_{\mathbf{r}_i}^{\mathbf{r}_j} \mathbf{A} \cdot \mathbf{dl} \right)$$

with the hoping energy $t = -2.7$ eV. In this paper we consider the magnetic field perpendicular to the graphene surface $\mathbf{B} = (0,0,B)$ and use the Landau gauge $\mathbf{A} = (-By,0,0)$. In order to model samples of linear size of about 300 nm we apply the
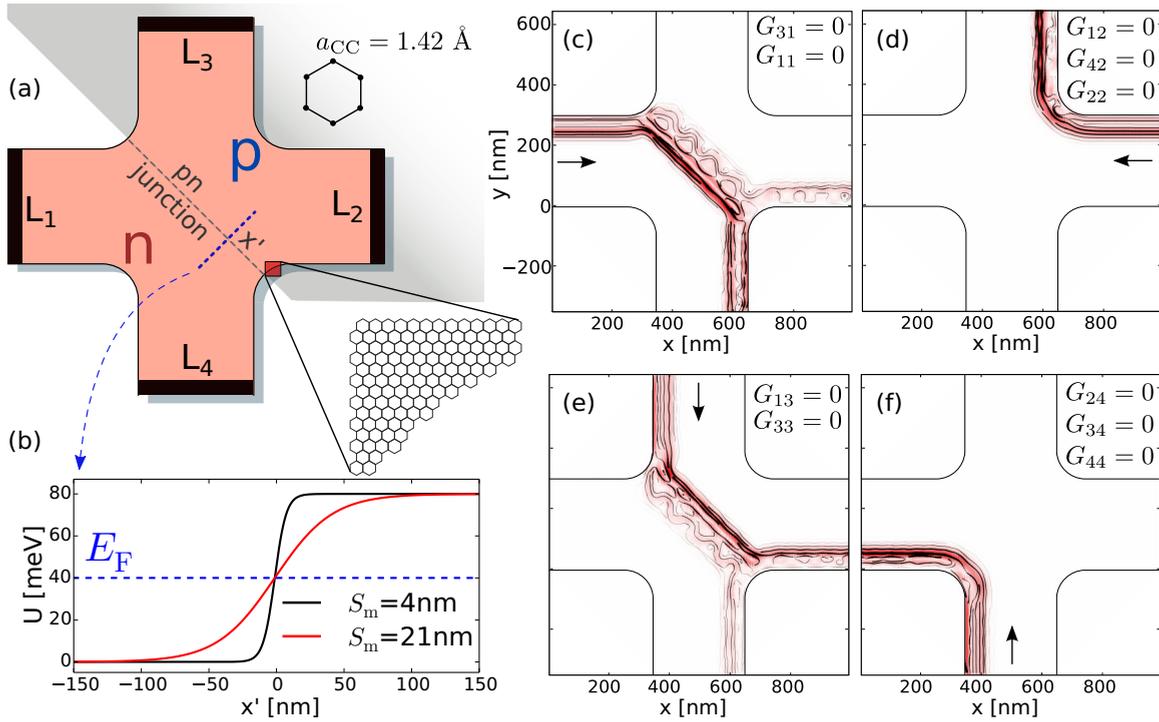
FIG. 1. (a) The sketch of the four-terminal device. The source and drain leads are denoted by L_1 and L_2 labels, respectively. L_3 and L_4 leads are voltage probes. The gray dashed line denotes the n-p junction induced by an external potential. (b) The potential profiles along the blue line in (a) for $S_m = 4$ nm and $S_m = 21$ nm modeled with Eq. (2). The n region is located to the left from the n-p interface. (c)–(f) The probability current maps obtained for electrons incoming from each of the leads L_i (incident direction is denoted by the black arrow). The maps are computed for $B = 1.3$ T, $E_F = eV_{PNJ}/2 = 40$ meV.

scaling method proposed in Ref. [46] with the scaling factor of 10.

We consider a system in which the n-p junction is formed by external potentials induced by the gate electrodes along the diagonal of the cross junction. The potential profile of the junction is modeled with an analytical formula

$$U_{PNJ}(x) = \frac{eV_{PNJ}}{e^{-x'/S_m} + 1}, \quad (2)$$

where the x' axis coincides with the $y = x$ line with the origin at the diagonal of the cross junction [see the dashed blue line in Figs. 1(a) and 1(b)]. In Eq. (2) eV_{PNJ} is the potential energy variation across the junction, and S_m controls the width of the n-p interface. The potential (2) for $eV_{PNJ} > E_F$ induces the n-p junction with the p-type conductivity in the upper-right part of the device of Fig. 1(a). In this paper we follow the choice of Ref. [25] and restrict our considerations to the symmetric case when the carrier densities are the same in the n- and p-type regions, i.e., for $eV_{PNJ} = 2E_F$.

In order to simulate the SGM mapping we use the Lorentzian approximation for the tip-induced potential

$$U_{tip}(\mathbf{r}; \mathbf{r}_{tip}) = \frac{d_{tip}^2 V_{tip}}{|\mathbf{r} - \mathbf{r}_{tip}|^2 + d_{tip}^2},$$

where $\mathbf{r}_{tip}$ is the position of the tip, d_{tip} is the Lorentzian width, and V_{tip} is the tip-induced amplitude. The tip-induced potential is controlled by external voltages, and its width is close to the distance between the tip and the sheet that confines the electron gas [47]. Here, we choose $d_{tip} = 25$ nm. The potential energy

$U_{tip}(\mathbf{r}; \mathbf{r}_{tip})$ enters the on-site term of the Hamiltonian (1), i.e., $U = U_{tip} + U_{PNJ}$.

In the experimental implementation of the mapping that is considered here, the main challenge seems to rely in a simultaneous formation of the n-p junction by electrostatic gating and the scanning gate microscopy of the sample. The gate electrons that form the n-p junction are usually deposited on top of the structure [41] and hence they are bound to screen the electrostatic potential of the tip exactly at the position of the n-p junction. A solution to this problem was provided recently with the system of split gates defined under the graphene plane, for which the n-p junctions are open for the action of the floating probe [48]. The graphene suspended above the gates [25] is also accessible for the scanning gate operation.

B. Conductance

In order to evaluate the transport properties of the device we use the Landauer-Büttiker approach together with the wave function matching method [49,50] which requires a numerical solution of the scattering problem. A low temperature ~ 0 K and a source-drain bias within the linear response regime are assumed.

The probability currents obtained for $B = 1.3$ T, $E_F = 40$ meV, and electrons incident from different leads are shown in Figs. 1(c)–1(f), with snakelike trajectories in Figs. 1(c) and 1(e). Note that already for this magnetic field value (i) the current flows only near the edges [51] and along the n-p junction and (ii) backscattering to the input lead is absent.

The conductance from lead p to q denoted as G_{qp} is computed from the Landauer formula

$$G_{qp} = G_0 \sum_{m,n} \left| T_{p,m}^{q,n} \right|^2, \qquad (3)$$

where $T_{p,m}^{q,n}$ is the scattering transmission amplitude with which an electron entering the device at lead p in mode m will leave the device at lead q in mode n. The summation runs over all propagating modes in the leads and G_0 stands for the conductance quantum $G_0 \equiv \frac{2e^2}{h}$. For more details about the applied computational method see, e.g., [49,50,52].

The conductance matrix **G** elements [53] for the four-terminal device are determined from solution of the scattering problem according to Eq. (3),

$$\mathbf{G} = \begin{pmatrix} g_{11} & -G_{12} & -G_{13} & -G_{14} \\ -G_{21} & g_{22} & -G_{23} & -G_{24} \\ -G_{31} & -G_{32} & g_{33} & -G_{34} \\ -G_{41} & -G_{42} & -G_{43} & g_{44} \end{pmatrix}$$

with $g_{ii} = \sum_{j \neq i} G_{ij}$.

In the quantum Hall conditions some elements of this matrix are zero [see Figs. 1(c)–1(f)]. In our device the quantum Hall edge transport appears for $B \gtrsim 0.8$ T, and then the conductance matrix acquires the form

$$\mathbf{G} = \begin{pmatrix} G_{14} & 0 & 0 & -G_{14} \\ -G_{21} & G_{21}+G_{23} & -G_{23} & 0 \\ 0 & -G_{32} & G_{32} & 0 \\ -G_{41} & 0 & -G_{43} & G_{41}+G_{43} \end{pmatrix}.$$

Additionally, we have $G_{23} + G_{43} = G_{32} = \nu_p$ and $G_{21} + G_{41} = G_{14} = \nu_n$ with $\nu_{p/n}$ being the spin-degenerated filling factors in the p/n regions. In the linear transport conditions the current in each of the leads is given by $\mathbf{I} = \mathbf{GV}$ for a given bias. We choose L_1 and L_2 to be source-drain electrodes, with the source $V_1 = V_S$ and the drain $V_2 = V_D$ potentials, respectively. Terminals L_3 and L_4 are used as voltage probes, which amounts to $I_3 = I_4 = 0$ and so $I_1 = -I_2$ (the plus sign stands for the current that enters the device). The condition $I_3 = I_4 = 0$ immediately implies $V_3 = V_D$. This fact can be also deduced from Fig. 1(d)—the current from the drain terminal passes to L_3 without scattering. From the form of the second row of the **G** matrix, we have $I_2 = -G_{21}V_S + (G_{21}+G_{23})V_D - G_{23}V_D = G_{21}(V_D - V_S)$. Hence, in the quantum Hall conditions the current flow is determined uniquely by the G_{21} matrix element, which is studied in detail below.

III. RESULTS

A. Conductance oscillations due to snake orbits

Figure 2(a) shows the $G = G_{21}$ conductance as a function of the magnetic field and the Fermi energy. The result contains an oscillatory pattern—marked with the dashed rectangle—similar to the one found [25] experimentally and identified with formation of snake orbits along the n-p junction. The snake state oscillations are visible in a quite large range of both E_F and B. For further studies we fix the value of Fermi energy $E_F = 40$ meV and analyze the results as a function of magnetic field. The zoomed fragment of Fig. 2(a) near
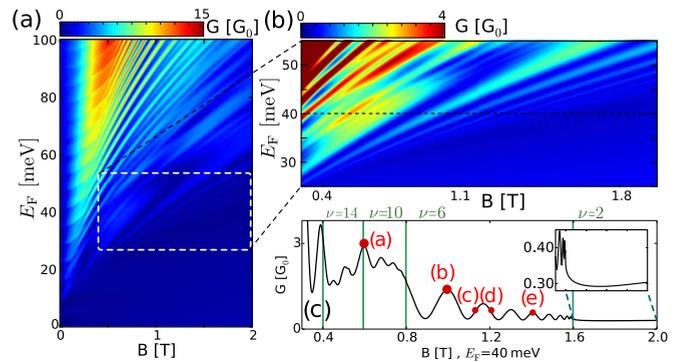
FIG. 2. (a) G_{21} conductance as a function of magnetic field B and Fermi energy $E_F = eV_{\text{PNJ}}/2$. (b) Zoom of the white rectangle in (a). (c) Cross section along the dashed line in (b). The red labels correspond to the SGM images in Figs. 3(a)–3(e). The filling factors in the channels are given above the plot and the inset to the right shows the zoom of conductance in the high magnetic field limit.

$E_F = 40$ meV is depicted in Fig. 2(b) and the cross section of the plot for $E_F = 40$ meV is given in Fig. 2(c).

Classically, these oscillations can be understood as due to the variation of the cyclotron orbits (with radius $R_c = \hbar k/eB$) as a function of B. The electron current can be then sent to either the L_2 or L_4 lead, depending on the value of R_c. Figures 3(a)–3(e) show the electron current distribution for the electron incident from the lead L_1 at $E_F = 40$ meV. The values of the external magnetic field are denoted by the corresponding letters in Fig. 2(c). Besides the current confinement along the n-p junction one notices deflection of the electron paths, in particular in the p-type (upper right) region of the device, with a radius that decreases with the external magnetic field.

In terms of the quantum transport theory, the snake orbits along the n-p junction—similarly to the skipping orbits [40] near the edge of the sample—appear as a result of the superposition of Landau level states

$$S(x,y) = \sum_{m=1}^{M_L} a_m e^{ik_{m}x} \chi_m(y), \qquad (4)$$

where k_m and χ_m denote the mth Fermi level wave vector and the corresponding transverse mode, respectively. The scattering amplitudes a_m depend on specific boundary conditions.

For simplicity let us assume that the particle is propagating along the x direction. For the case when $M_L = 1$ the electron density $|S(x,y)|^2 = |a_1 \chi_1(y)|^2$ does not depend on x and there is no room for the density variation along the edge or the junction. In this case the idea of the classical cyclotron orbit is irrelevant. For superposition of two or more modes the $|S(x,y)|^2$ density results from a superposition of modes with different Fermi wave vectors, leading to the oscillating pattern.

Figure 4(a) shows the dispersion relation for a horizontal channel in lead L_1 which is denoted by the green arrow in the inset. For $B = 1.2$ T there are three modes which are propagating to the right (green dots) and three modes for opposite direction (red dots). The wave vectors k_i can be computed from condition $E_i(k_i) = E_F$ [49,52]. In Fig. 4(b) we show the dispersion relation for a channel created along the n-p junction of width $S_m = 4$ nm (see the inset). For

FIG. 3. (a)–(e) Probability current distribution in the absence of the scanning probe (left column) and (f)–(j) SGM images (right column) for magnetic fields $B = 0.6, 1, 1.14, 1.2, 1.4$ T that are indicated in Fig. 2(c).
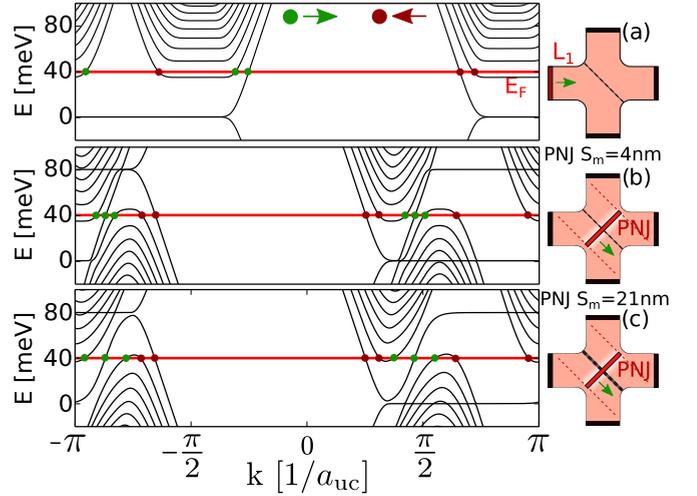
FIG. 4. (a) Electron dispersion relation for the lead L_1. The green and red dots denote the Fermi level wave vectors for the right- and the left-moving modes, respectively. (b) Same as (a) but computed for a channel along the n-p junction interface and for $S_m = 4$ nm. (c) Same as (b) but for a smoother junction $S_m = 21$ nm. a_{uc} is the length of the unit cell vector along which the dispersions are computed. The results were calculated for $B = 1.2$ T and $E_F = 40$ meV.

the Bogoliubov quasiparticles and can be explained as a result of coupling the n-type and the p-type conductivity regions, in this case with three conduction and three valence bands at each side of the junction.

We find that the state doubling is not always present in smooth junctions of a finite width; see, e.g., Figs. 4(b) and 4(c) where a small shift of the Fermi energy line will decrease the number of right-moving modes from 6 to 4. The slope of the energy bands as function of the width of the junction S_m changes: the plateaus at the extrema of the bands get narrower in k [cf. the bottoms of the bands in Figs. 4(b) and 4(c)] for increased S_m, which results in particular in a stronger dependence of the Fermi wave vectors on both E_F and B off the band extrema. In Fig. 5(a) we show the evolution of the first six Fermi k_i wave vectors for right-moving modes as a function of magnetic field. The black lines correspond to $S_m = 4$ nm.

The conductance oscillations of Fig. 2(c) can be explained by the superposition of the modes propagating along the junction. We consider the Fermi wave vectors and look for the closest pair of k's that correspond to the positive velocity $dE/dk > 0$. A superposition [see Eq. (4)] of these two modes produces a charge density variation of the largest wavelength $\lambda_{max} = 2\pi/k_{min}$,

$$k_{min} \equiv \min_{i,j} |k_i - k_j|. \tag{5}$$

Within the range of the magnetic field from $B = 0.8$ T to 1.6 T the minimal distance between the right-going wave vectors appears for the two lowest ones in Fig. 5(a) and the two highest ones. Both distances are found equal. For a superposition of the two modes with the closest wave vectors $S = a_i \exp(ik_i x)\chi_1(y) + a_j \exp(ik_j x)\chi_2(y)$. Hence the charge density along the junction can be put in a form $|S|^2 = |a_i|^2|\chi_i(y)|^2 + |a_j|^2|\chi_j(y)|^2 + 2\text{Re}(a_i^* a_j)\chi_i^*(y)$

the junction the number of right-propagating Landau levels is now doubled (six right and six left propagating modes). The doubling of the states in the n-p junction was recently discussed for steplike junctions in Ref. [26] with reference to
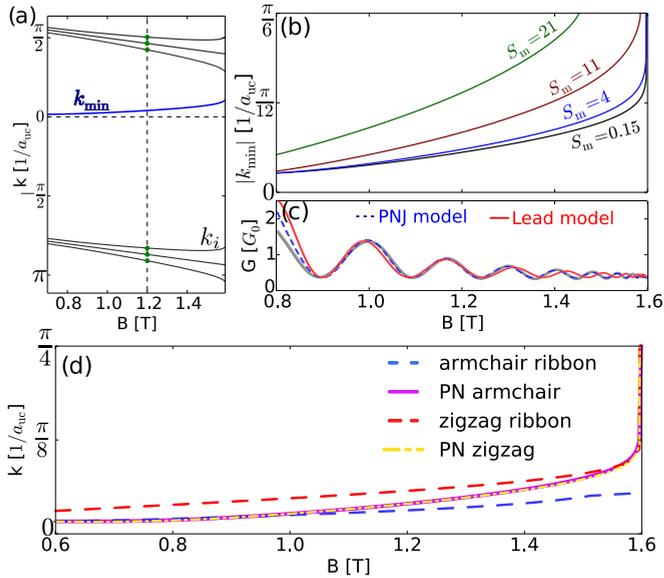
FIG. 5. (a) Black lines show the wave vectors k_i for the right-going modes at the Fermi level of the n-p junction interface from Fig. 4(b). The vertical dashed line corresponds to Fig. 4(b); see the green dots in both the plots. The blue line shows the calculated k_{min} values according to Eq. (5). (b) $k_{min}(B)$ [see Eq. (5)] for different values of the junction smoothness parameter S_m. (c) The gray solid line, the exact result; the blue dashed line (PNJ model), the best fit obtained from formula (6) for the dispersion relation of the n-p junction as a conducting channel; the red line, the best fit obtained for the wave vectors of the energy bands of the input lead L_1. (d) The value of k_{min} plotted for armchair and zigzag ribbons (dashed curves)—in the leads of Fig. 1(a) as well as for the n-p junction; dash-dotted curve and solid curve for a zigzag and an armchair ribbon with the n-p junction defined along its axis with $S_m = 4$ nm.

$\chi_j(y) - 4\mathrm{Re}(a_1^* a_2) \sin^2(\frac{(k_i - k_j)x}{2}) \chi_i^*(y) \chi_j(y)$. The last term is responsible for the oscillations of the density along the junction, and the G_{21} conductance depends on the destination of the current that reaches the end of the n-p junction at its contact with the edge. At that point the electron current reaches either L_4 or L_2. The oscillations of Fig. 2(c) can be described by a a simple phenomenological formula

$$G(B) = a + be^{-cB} \sin^2 \left(\frac{k_{min}(B)L}{2} \right), \qquad (6)$$

where the exponential part accounts for the observed decay of the oscillations at high B and $L = 455$ nm is the length of the junction.

The decrease of the amplitude for higher magnetic field can be understood based on the recent Ref. [8], which shows that the transmission coefficient for electron traveling through the n-p junction of a finite width is below 1. Here we consider the junction with $S_m = 4$ nm which according to Ref. [8] gives the transmission probability ~ 0.5. Now, if we increase the magnetic field the number of times that the electron passes across the n-p interface increases, hence the reduction of the conductance oscillation amplitude.

Figure 2(c) shows that the conductance oscillations vanish in the strong external magnetic field limit that reduces the

filling factor to $\nu = 2$, i.e., when a single subband with the spin degree of freedom is present. Above 1.6 T, the conductance only depends on the external magnetic field. The results indicate a nearly constant value near 0.3 G_0, which is close to the 0.25 G_0 value obtained in Ref. [6] by both the continuum approximation and the tight-binding model for the armchair nanoribbon with a perpendicular n-p junction. For the present geometry the high magnetic field limit is not exactly a plateau, and the conductance variation is observed; see the inset to Fig. 2(c).

The results of the fit with formula (6) for the dispersion relation for the n-p junction [Fig. 4(b)] are denoted as the "PNJ model" in Fig. 5(c)—the dashed blue line, which above 0.9 T agrees perfectly with the numerical conductance. A similar analysis was performed in Ref. [24] but for the dispersion relation of the input lead and not the n-p junction itself. The fit for the dispersion relation of the input lead is given by the red line in Fig. 5(c), in which the agreement is not as good as for the "PNJ model." Note that the fit becomes even worse for a larger magnetic field, where the out-of-phase range is visible. A distinct shift can also be spotted in Fig. 4(f) of Ref. [24] between the model and numerical values, however at lower B. The present result indicates that the properties of the band structure of the n-p junction as the conducting channel precisely determine the period of the conductance oscillations on the magnetic field scale in the quantum Hall conditions.

Figure 5(c) shows the value of k_{min} as calculated for the armchair and the zigzag ribbons—without the external potential variation—as well as the ribbons in which the n-p junction is defined along its symmetry axis. The later case corresponds to the graphene band marked by dashed red lines in Fig. 4(c). For the ribbon with the n-p junction along its axis the current is confined along the junction and ignores the form of the edge of the ribbon, which makes the results for the snake states independent of the details of the structure outside the junction itself. The figure shows that for the ribbon without the external potential the value of k_{min} highly depends on the ribbon edge; hence the fit of Eq. (6) depends on the type of the edge, which is not the case for the ribbons with the n-p junction.

B. Imaging the snake states

1. Weak perturbation

As weak perturbation we consider the tip potential of $V_{tip} = 10$ meV—four times smaller than the Fermi energy. In Figs. 3(f)–3(i) we show the SGM conductance maps for the current distribution given in the left column in Figs. 3(a)–3(e).

The conductance does react to the external perturbation—but only for the scanning probe near the n-p junction. No effect is observed for the tip in the leads. The tip deflects the trajectory to L_4 or L_2 leads but no backscattering is present which is characteristic to the quantum Hall conditions, hence the flat maps for the probe above the leads.

Figures 3(a) and 3(f) correspond to the magnetic field where a conductance peak [Fig. 5(c)] is observed. For this magnetic field the cyclotron radius is comparable to the length of the n-p junction. The SGM image [Fig. 2(f)] does not resolve the details of this orbit. Moreover, here and for other B values the SGM maps have an approximate symmetry with
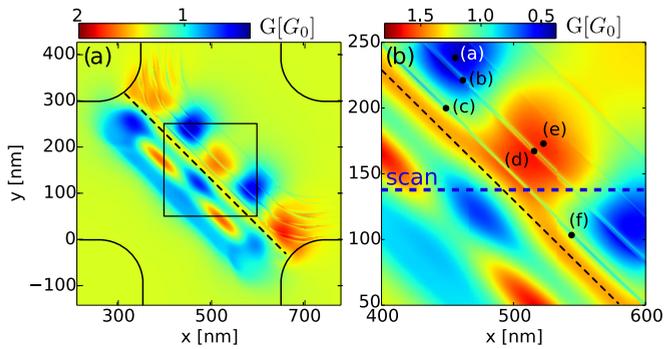
FIG. 6. (a) The conductance map for $V_{tip} = 30$ meV and $B = 1$ T. (b) The zoom of the black rectangle in (a). The labels correspond to tip locations considered in Fig. 7.

respect to the inversion through the bisector of the junction (here $y = x$ line) which is missing in the current plots.

For the subsequent conductance peak marked by "b)" in Fig. 2(c) the cyclotron radius of the deflected electron trajectory [Fig. 5(c)] is already $\simeq 5$ times shorter than L [see Fig. 3(b)] and the distance between the extrema of conductance map [Fig. 3(g)] along the junction is comparable to the cyclotron radius. This also found for higher magnetic fields—Figs. 3(c) and 3(h), 3(d) and 3(i), and 3(e) and 3(j)—although the visibility of the oscillation becomes unequal at the opposite sides of the junction. The nontransparency of the finite-width junction for electrons [8], discussed in the context of Fig. 5(c), is one of the possible reasons responsible for the reduction of the conductance visibility at high magnetic field.

For magnetic fields above 1.6 T which correspond to the filling factor of $\nu = 2$ [see Fig. 2(c)], the conductance maps resolve only the contact of the n-p junction to the edge where opposite extrema are found on both ends of the junction [the effect is already visible in Fig. 3(e)] and the conductance variation along the junction far from the edges disappears.

2. Strong perturbation

The SGM images for a stronger tip potential $V_{tip} = 30$ meV and $B = 1$ T are displayed in Fig. 6—to be compared with Fig. 3(b) for $V_{tip} = 10$ meV. The asymmetry of the plot between the n and p sides of the junction is increased for larger V_{tip}. Moreover, a number of resonances is found at the p side at lines parallel to the junction. The current density plots for tip location over the points indicated in Fig. 6(b) are displayed in Fig. 7. The resonances are related to current loops that encircle the tip. The current loops are found for the tip on the p side only. The tip potential repels the carriers on the conduction band side of the junction. The currents on the n side simply avoid the perturbation and no loop of current is found. For the carriers on the valence band side the potential maximum induced by V_{tip} is attractive and thus it supports a quasibound state. The exact positions of the resonances depend on the magnetic field in a periodic manner, which is related to the Aharonov-Bohm effect for the current circulation around the tip that couples to the junction current. The conductance across the junction is displayed in Fig. 8 along the dashed line marked in Fig. 6(a) as a function of the external magnetic field.
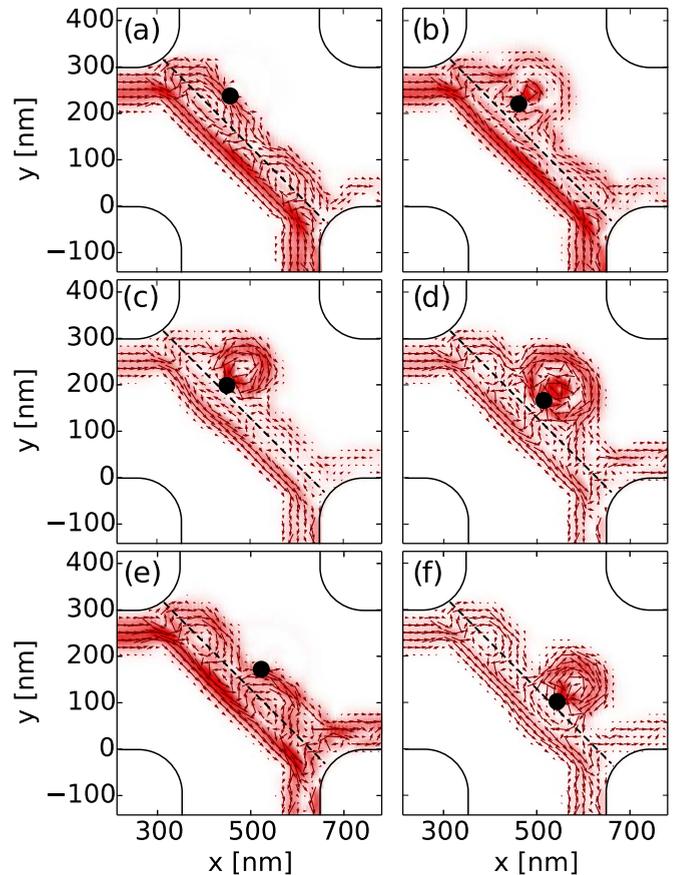
FIG. 7. Probability current distribution obtained for the probe locations denoted in Fig. 6(b).

For lower magnetic fields the resonances are found also for the tip near the n-p junction on the n side. For a given tip location the spacing between the subsequent resonances depends on the magnetic field. For higher magnetic fields the clockwise loop that is seen in Fig. 7 is made tighter by the Lorentz force which acts to the right of the current orientation on the p conductivity side. For a reduced radius of the current loop the magnetic field period corresponding to a flux quantum is increased.
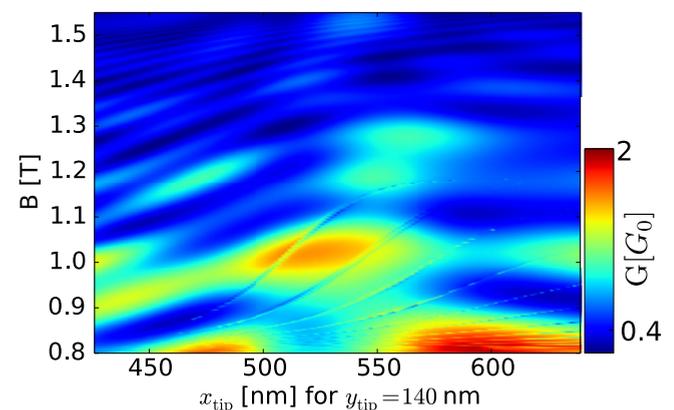
FIG. 8. The conductance along the horizontal dashed line in Fig. 6(b) as a function of the magnetic field.
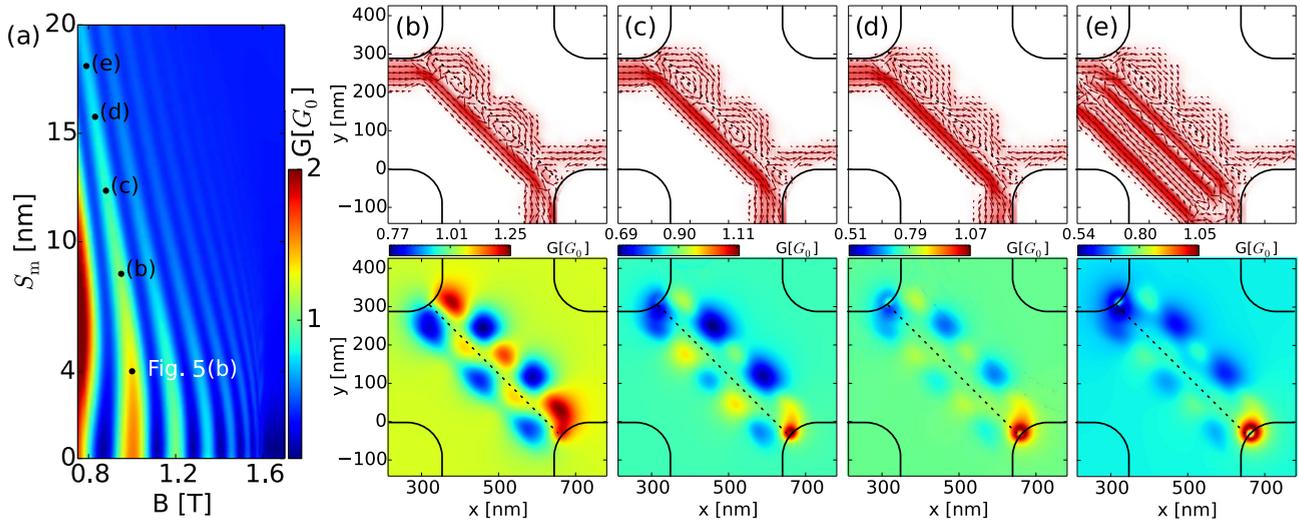
FIG. 9. (a) The conductance as a function of magnetic field and the junction smoothness parameter S_m. The white label corresponds to the case shown in Fig. 5(b). (b)–(e) The probability current distribution and the corresponding conductance maps for the work points marked in (a).

C. Conductance maps for wider *n*-*p* junctions

So far we have discussed the case of a thin junction with $S_m = 4$ nm. From the discussion in Sec. III A we know that the width of the junction strongly affects the dispersion relation. We calculated the conductance at $E_F = 40$ meV [as in Fig. 2(c)] as a function of the junction width S_m and the magnetic field. In the result presented in Fig. 9(a) one notices that (i) the resonance lines bend towards lower magnetic field as S_m is increased and (ii) the amplitude of the oscillations decreases with S_m. The feature (i) results from the fact that the spacing between the nearest k vectors is increased for wider junctions and at higher magnetic field [Fig. 5(b)]. The corresponding resonances appear for smaller magnetic field values at larger S_m. The finding (ii) seems due to a decreased transparency of the junction with its width found recently in Ref. [8]. To summarize, we find that for a smooth junction snake orbits appear for lower magnetic fields but at the expense of the visibility of oscillations.

Figures 9(b)–9(e) show the probability current plots and SGM conductance maps for the work points marked in Fig. 9(a) and $V_{tip} = 10$ meV along a selected resonance line. One may see that once we increase S_m the snake features become less resolved both in the current plots and the conductance maps. The current along the n side increases with S_m. The deflected trajectories remain at the p side, where also the amplitude of the conductance map remains stronger than on the n side. In Fig. 9(e) the number of spin-degenerated modes is 5 instead of 3; hence the current plot contains additional features from higher modes. However, in the corresponding SGM image no additional features are found.

IV. SUMMARY AND CONCLUSIONS

We have discussed the conductance mapping of the snake orbits confined at the n-p junction in graphene. We indicated a precise relation of the conductance oscillations at the magnetic field scale with the Fermi wavelengths of the n-p junction as a waveguide. We found that the maps of conductance contain oscillating patterns along the junction with a period of the oscillation that is close to the period of the snake orbit. The visibility of the map decreases with the external magnetic field due to an increased number of the electron passages across the junction and a nonideal transparency of the n-p junction of a finite width. The conductance maps are found to be nearly symmetrical across the bisector of the junction with an asymmetry between the n and p sides. For stronger tip potentials resonant quasibound states are formed under the tip at one of the junction sides. The interference of the quasibound states with the junction currents produces resonances parallel to the junction with positions that react strongly to the external magnetic field via the Aharonov-Bohm phase shift. We demonstrated that the width of the n-p interface affects the oscillation period and the visibility of the conductance maps.

[1] A. H. Castro Neto, F. Guinea, N. M. R. Peres, K. S. Novoselov, and A. K. Geim, Rev. Mod. Phys. **81**, 109 (2009).

[2] K. Bolotin, K. Sikes, Z. Jiang, M. Klima, G. Fudenberg, J. Hone, P. Kim, and H. Stormer, Solid State Commun. **146**, 351 (2008).

[3] L. Banszerus, M. Schmitz, S. Engels, M. Goldsche, K. Watanabe, T. Taniguchi, B. Beschoten, and C. Stampfer, Nano Lett. **16**, 1387 (2016).

[4] T. K. Ghosh, A. De Martino, W. Häusler, L. Dell'Anna, and R. Egger, Phys. Rev. B **77**, 081404 (2008).

[5] D. A. Abanin and L. S. Levitov, Science **317**, 641 (2007).

[6] J. Tworzydło, I. Snyman, A. R. Akhmerov, and C. W. J. Beenakker, Phys. Rev. B **76**, 035411 (2007).

[7] V. V. Cheianov, V. Fal'ko, and B. L. Altshuler, Science **315**, 1252 (2007).

[8] S. Chen, Z. Han, M. M. Elahi, K. M. M. Habib, L. Wang, B. Wen, Y. Gao, T. Taniguchi, K. Watanabe, J. Hone, A. W. Ghosh, and C. R. Dean, Science **353**, 1522 (2016).

[9] P. Rickhaus, R. Maurand, M.-H. Liu, M. Weiss, K. Richter, and C. Schönenberger, Nat. Commun. **4**, 2342 (2013).

[10] T. Taychatanapat, J. Y. Tan, Y. Yeo, K. Watanabe, T. Taniguchi, and B. Özyilmaz, Nat. Commun. **6**, 6093 (2015).

[11] G.-H. Lee, G.-H. Park, and H.-J. Lee, Nat. Phys. **11**, 925 (2015).

[12] M.-H. Liu, C. Gorini, and K. Richter, arXiv:1608.01730.

[13] J. R. Williams, L. DiCarlo, and C. M. Marcus, Science **317**, 638 (2007).

[14] B. Huard, J. A. Sulpizio, N. Stander, K. Todd, B. Yang, and D. Goldhaber-Gordon, Phys. Rev. Lett. **98**, 236803 (2007).

[15] B. Özyilmaz, P. Jarillo-Herrero, D. Efetov, D. A. Abanin, L. S. Levitov, and P. Kim, Phys. Rev. Lett. **99**, 166804 (2007).

[16] J. R. Williams, T. Low, M. S. Lundstrom, and C. M. Marcus, Nat. Nanotechnol. **6**, 222 (2011).

[17] M. Barbier, G. Papp, and F. M. Peeters, Appl. Phys. Lett. **100**, 163121 (2012).

[18] N. Davies, A. A. Patel, A. Cortijo, V. Cheianov, F. Guinea, and V. I. Fal'ko, Phys. Rev. B **85**, 155433 (2012).

[19] J. R. Williams and C. M. Marcus, Phys. Rev. Lett. **107**, 046602 (2011).

[20] P. Carmier, C. Lewenkopf, and D. Ullmo, Phys. Rev. B **84**, 195428 (2011).

[21] J.-C. Chen, X. C. Xie, and Q.-F. Sun, Phys. Rev. B **86**, 035429 (2012).

[22] A. Cresti, G. Grosso, and G. P. Parravicini, Phys. Rev. B **77**, 233402 (2008).

[23] S. P. Milovanović, M. Ramezani Masir, and F. M. Peeters, J. Appl. Phys. **115**, 043719 (2014).

[24] S. P. Milovanović, M. Ramezani Masir, and F. M. Peeters, Appl. Phys. Lett. **105**, 123507 (2014).

[25] P. Rickhaus, P. Makk, M.-H. Liu, E. Tóvári, M. Weiss, R. Maurand, K. Richter, and C. Schönenberger, Nat. Commun. **6**, 6470 (2015).

[26] Y. Liu, R. P. Tiwari, M. Brada, C. Bruder, F. V. Kusmartsev, and E. J. Mele, Phys. Rev. B **92**, 235438 (2015).

[27] M. Zarenia, J. M. Pereira, F. M. Peeters, and G. A. Farias, Phys. Rev. B **87**, 035426 (2013).

[28] L. Oroszlány, P. Rakyta, A. Kormányos, C. J. Lambert, and J. Cserti, Phys. Rev. B **77**, 081403 (2008).

[29] J. E. Müller, Phys. Rev. Lett. **68**, 385 (1992).

[30] B. Szafran and F. M. Peeters, Europhys. Lett. **70**, 810 (2005).

[31] M. A. Topinka, B. J. LeRoy, S. E. J. Shaw, E. J. Heller, R. M. Westervelt, K. D. Maranowski, and A. C. Gossard, Science **289**, 2323 (2000).

[32] M. A. Topinka, B. J. LeRoy, R. M. Westervelt, S. E. J. Shaw, R. Fleischmann, E. J. Heller, K. D. Maranowski, and A. C. Gossard, Nature (London) **410**, 183 (2001).

[33] A. A. Kozikov, R. Steinacher, C. Rössler, T. Ihn, K. Ensslin, C. Reichl, and W. Wegscheider, Nano Lett. **15**, 7994 (2015).

[34] M. P. Jura, M. A. Topinka, M. Grobis, L. N. Pfeiffer, K. W. West, and D. Goldhaber-Gordon, Phys. Rev. B **80**, 041303 (2009).

[35] H. Sellier, B. Hackens, M. G. Pala, F. Martins, S. Baltazar, X. Wallart, L. Desplanque, V. Bayot, and S. Huant, Semicond. Sci. Technol. **26**, 064008 (2011).

[36] S. Morikawa, Z. Dou, S.-W. Wang, C. G. Smith, K. Watanabe, T. Taniguchi, S. Masubuchi, T. Machida, and M. R. Connolly, Appl. Phys. Lett. **107**, 243102 (2015).

[37] S. Bhandari, G.-H. Lee, A. Klales, K. Watanabe, T. Taniguchi, E. Heller, P. Kim, and R. M. Westervelt, Nano Lett. **16**, 1690 (2016).

[38] V. E. Calado, S.-E. Zhu, S. Goswami, Q. Xu, K. Watanabe, T. Taniguchi, G. C. A. M. Janssen, and L. M. K. Vandersypen, Appl. Phys. Lett. **104**, 023103 (2014).

[39] P. Rakyta, A. Kormányos, J. Cserti, and P. Koskinen, Phys. Rev. B **81**, 115411 (2010).

[40] T. Stegmann and A. Lorke, Ann. Phys. (Berlin) **527**, 723 (2015).

[41] T. Taychatanapat, K. Watanabe, T. Taniguchi, and P. Jarillo-Herrero, Nat. Phys. **9**, 225 (2013).

[42] S. Weingart, C. Bock, U. Kunze, F. Speck, T. Seyller, and L. Ley, Appl. Phys. Lett. **95**, 262101 (2009).

[43] J. Du, J. Y. Li, N. Kang, L. Lin, H. Peng, Z. Liu, and H. Q. Xu, Nanotechnology **27**, 245204 (2016).

[44] A. S. Mayorov, R. V. Gorbachev, S. V. Morozov, L. Britnell, R. Jalil, L. A. Ponomarenko, P. Blake, K. S. Novoselov, K. Watanabe, T. Taniguchi, and A. K. Geim, Nano Lett. **11**, 2396 (2011).

[45] L. Cohnitz, A. D. Martino, W. Häusler, and R. Egger, Phys. Rev. B **94**, 165443 (2016).

[46] M.-H. Liu, P. Rickhaus, P. Makk, E. Tóvári, R. Maurand, F. Tkatschenko, M. Weiss, C. Schönenberger, and K. Richter, Phys. Rev. Lett. **114**, 036601 (2015).

[47] B. Szafran, Phys. Rev. B **84**, 075336 (2011).

[48] S. Xiang, A. Mrenca-Kolasinska, V. Miseikis, S. Guiducci, K. Kolasinski, C. Coletti, B. Szafran, F. Beltram, S. Roddaro, and S. Heun, Phys. Rev. B **94**, 155446 (2016).

[49] H. H. B. Sørensen, P. C. Hansen, D. E. Petersen, S. Skelboe, and K. Stokbro, Phys. Rev. B **79**, 205322 (2009).

[50] K. Kolasiński, B. Szafran, B. Brun, and H. Sellier, Phys. Rev. B **94**, 075301 (2016).

[51] R. J. Haug, Semicond. Sci. Technol. **8**, 131 (1993).

[52] M. Zwierzycki, P. A. Khomyakov, A. A. Starikov, K. Xia, M. Talanana, P. X. Xu, V. M. Karpan, I. Marushchenko, I. Turek, G. E. W. Bauer, G. Brocks, and P. J. Kelly, Phys. Status Solidi B **245**, 623 (2008).

[53] S. Datta, *Electronic Transport in Mesoscopic Systems* (Cambridge University Press, Cambridge, 1997).